

# Laser-Induced Tar-Mediated Sintering of Metals and Refractory Carbides in Air

Xining Zang, Kiera Y. Tai, Cuiying Jian, Wan Shou, Wojciech Matusik, Nicola Ferralis, and Jeffrey C. Grossman\*



Cite This: <https://dx.doi.org/10.1021/acsnano.0c04295>



Read Online

ACCESS |



Metrics & More



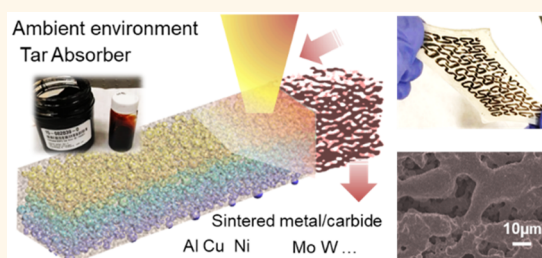
Article Recommendations



Supporting Information

**ABSTRACT:** Refractory metals and their carbides possess extraordinary chemical and temperature resilience and exceptional mechanical strength. Yet, they are notoriously difficult to employ in additive manufacturing, due to the high temperatures needed for processing. State of the art approaches to manufacture these materials generally require either a high-energy laser or electron beam as well as ventilation to protect the metal powder from combustion. Here, we present a versatile manufacturing process that utilizes tar as both a light absorber and antioxidant binder to sinter thin films of aluminum, copper, nickel, molybdenum, and tungsten powder using a low power (<2W) CO<sub>2</sub> laser in air. Films of sintered Al/Cu/Ni metals have sheet resistances of  $\sim 10^{-1}$  ohm/sq, while laser-sintered Mo/W-tar thin films form carbide phases. Several devices are demonstrated, including laser-sintered porous copper with a stable response to large strain (3.0) after 150 cycles, and a laserprocessed Mo/MoC<sub>(1-x)</sub> filament that reaches  $T \sim 1000$  °C in open air at 12 V. These results show that tar-mediated laser sintering represents a possible low energy, cost-effective route for engineering refractory materials and one that can easily be extended to additive manufacturing processes.

**KEYWORDS:** steam cracker tar, laser sintering, transition metal, refractory metal carbides, laser manufacturing



Refractory metals such as molybdenum, tungsten, and their carbides possess extraordinary chemical and thermal resilience and mechanical strength.<sup>1,2</sup> Tungsten and molybdenum carbide have been widely applied in machine tools and armor-piercing shells,<sup>3</sup> and their alloys have been applied in parts of aeronautical engines including nozzles and turbine blades.<sup>4</sup> However, they can be difficult to engineer due to their high melting temperatures.<sup>5–7</sup> Unlocking low-cost processing conditions for sintering and printing methods using refractory materials could lead to additive manufacturing processes and applications, from biomedical engineering,<sup>8</sup> to power plants,<sup>9</sup> to aerospace.<sup>10</sup>

Laser annealing has been shown to provide low-cost versatile thermal processing methods with broad material compatibility and spatial resolution.<sup>11–14</sup> In addition to controlling laser-specific parameters such as power, rastering speed, and focus, material synthesis paradigms can be developed by exploiting light-matter interactions to enhance and localize thermal transformations.<sup>15</sup> State-of-the-art additive manufacturing methods such as selective laser melting (SLM) and electron beam melting (EBM) require relatively high laser power (up to several kilowatts) while operating under vacuum or inert gas.<sup>16</sup> Direct additive manufacturing (3D printing) of ceramics and refractory, high entropy alloys is generally difficult due to their high melting temperatures and the challenge of controlling

phase transformation during the thermal processes.<sup>10,17</sup> One approach that has been used recently includes printing polymer based precursors followed by a postcombustion process: a silicon oxycarbide microlattice can be derived from preceramic polymers; an alloy of Al–Co–Cr–Fe–Ni can be reduced by annealing in CO from a 3D structure printed using a polymer blend with oxide nanopowder.<sup>7,18</sup> These postconversion processes induce volume shrinking, porosity, and increase of impurities, and direct printing process have the potential to resolve these problems.

Herein, we present a versatile manufacturing process to sinter thin films of aluminum, copper, nickel, molybdenum, and tungsten, using the petroleum processing byproduct steam cracker tar (SCT) as a binder.<sup>12</sup> The adaptable viscosity of tar, combined with its enhanced light absorption properties and flexible chemistry, facilitates the direct patterning and laser sintering of metal microparticles into metal and metal carbide

**Received:** May 22, 2020

**Accepted:** August 3, 2020

**Published:** August 3, 2020

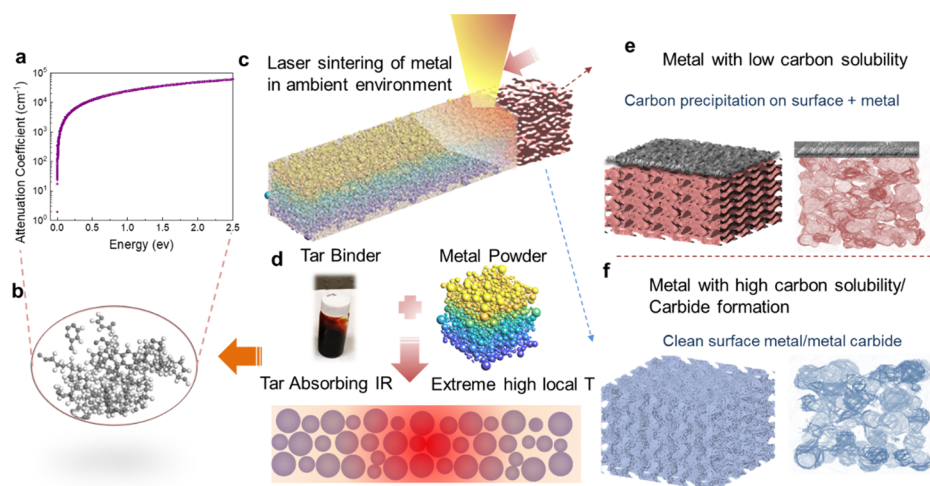


**Figure 1.** Schematic of laser annealing of metal and refractory metal carbides using petroleum tar as the light-absorbing binder, at ambient conditions. (a) Attenuation coefficient of tar model calculated by first-principles simulations. (b) Atomic model of tar. (c, d) Illustration of laser-sintered metal thin film with tar binder. (e) Carbon segregation on metals with low carbon solubility like aluminum and copper after laser sintering. (f) Metals with high carbon solubility lead to a smooth surface after sintering; refractory metals molybdenum and tungsten form carbides.

thin films in air without formation of oxides. Using tar as a light absorber and antioxidant enables direct sintering in air with a low power (<2W) CO<sub>2</sub> laser, rather than at the temperatures used in bulk annealing above melting temperatures (Table S1). Tar displays an attenuation coefficient ( $\sim 10^3$  cm<sup>-1</sup>) 2 orders of magnitude lower than that of metals ( $\sim 10^5$  cm<sup>-1</sup>) at the laser excitation wavelength (10.6  $\mu$ m),<sup>19–22</sup> resulting in a deeper penetration depth of the laser into the metal–tar thin film. Additionally, the lower attenuation coefficient of tar allows for higher efficiency in the photon to thermal energy conversion. By optimizing laser parameters and metal powder size distribution, we show that laser-treated metal/tar thin films produce metal phases (Al, Cu, Ni) and metal carbide phases (Mo, W) with low sheet resistance, as low as 10<sup>-1</sup> ohm/sq. As proofs of concept, a printed copper auxetic pattern is transferred onto Ecoflex to assemble a strain sensor with a gauge factor of  $\sim 20$ , and a printed molybdenum carbide thin film joule heater can reach over 1000 °C in open air. Furthermore, we successfully demonstrate the tar-mediated sequential vertical patterning of a double layer molybdenum carbide thin film, which indicates the potential suitability of this method for additive manufacturing with refractory carbides.

## RESULTS AND DISCUSSION

Steam cracker tar, the byproduct of ethylene cracking, is a combination of polycyclic aromatic hydrocarbons (PAHs) and alkanes (Figure 1a,b). Tar absorbs around 10  $\mu$ m due to the C–C vibration in PAH.<sup>23</sup> Using first-principles simulations, the attenuation coefficient of tar at 10.6  $\mu$ m ( $\sim 10^3$  cm<sup>-1</sup>), as shown in Figure 1a,b (see the details in Figure S1 and Table S2) is found to be much smaller than that of metals ( $\sim 10^5$  cm<sup>-1</sup>) (Table S1). Carbon materials such as a sparse vertical aligned carbon nanotube forest, carbon black, and graphite could function as near blackbody materials to increase the light absorptivity and emissivity.<sup>24</sup> The heavy polyaromatics in tar are transformed into a highly aromatic nanoscale framework during laser annealing, leading to the formation of nanoscale cavities acting as black-bodies with near-unity absorptivity,<sup>12</sup> similar to nanoscale cavity absorption enhancements observed

in carbon nanotubes.<sup>24</sup> Such a structural property could enhance the laser absorptivity and emissivity within the tar–metal and lead to higher internal temperatures. A tar solution (15 wt %) is made by diluting as received tar by dichloromethane (DCM). Thin films are synthesized by spin coating from a suspension of metal powder (1–5  $\mu$ m particle size) in tar solution with mass ratio 100:15:85 (metal/tar/solvent) (Figure 1c,d). The incident excitation laser power is found to be dissipated and reflected internally among the metal particles, allowing it to penetrate deeper and increase the light/metal power coupling.

As shown in Figure 1e,f and Figure 2, the structural conformation of sintered metal–tar thin films depends on two factors: the carbon solid solubility in the given metal and the formation energy of the corresponding metal carbide. In order to explore the roles of these two factors, five metals of varying carbon solubility and carbide formation energies were chosen: Al, Cu, Ni, Mo, and W. Aluminum has both a relatively low melting temperature ( $\sim 600$  °C) and low solid carbon solubility (0.015 wt %). Copper also possesses a very low carbon solid solubility,<sup>25</sup> which has been exploited to control the growth of monolayer graphene by chemical vapor deposition.<sup>26</sup> Ni has high carbon solubility and strong chemisorption binding with carbon atoms.<sup>27,28</sup> From the phase diagram of Mo–C and W–C, the values of formation energy of their respective carbides are even lower than melting Mo and W in the presence of carbon.<sup>29,30</sup> (Figure 2j,m and Figures S2–4). Phase segregation of carbon on the metal surface is not observed in laser annealed Ni–tar patterns from SEM images, which can be attributed to the high carbon solid solubility of C in Ni. On the other hand, a thin layer of amorphous carbon (<1/10 of film thickness) is always observed on the Cu-based sintered film, as shown in the energy-dispersive X-ray spectroscopy (EDX) mapping and Raman spectrum Figure S2. Similarly, a thin layer of carbon segregates to the surface of laser sintered Al–tar thin films (Figure S3). We note that the intensity of the X-ray diffraction (XRD) [2 0 0] reflection (52.4°, with a corresponding lattice distance of  $d = 2.02$  Å) increases with the power/speed ratio indicating a recrystallization of Al powder in the laser sintering

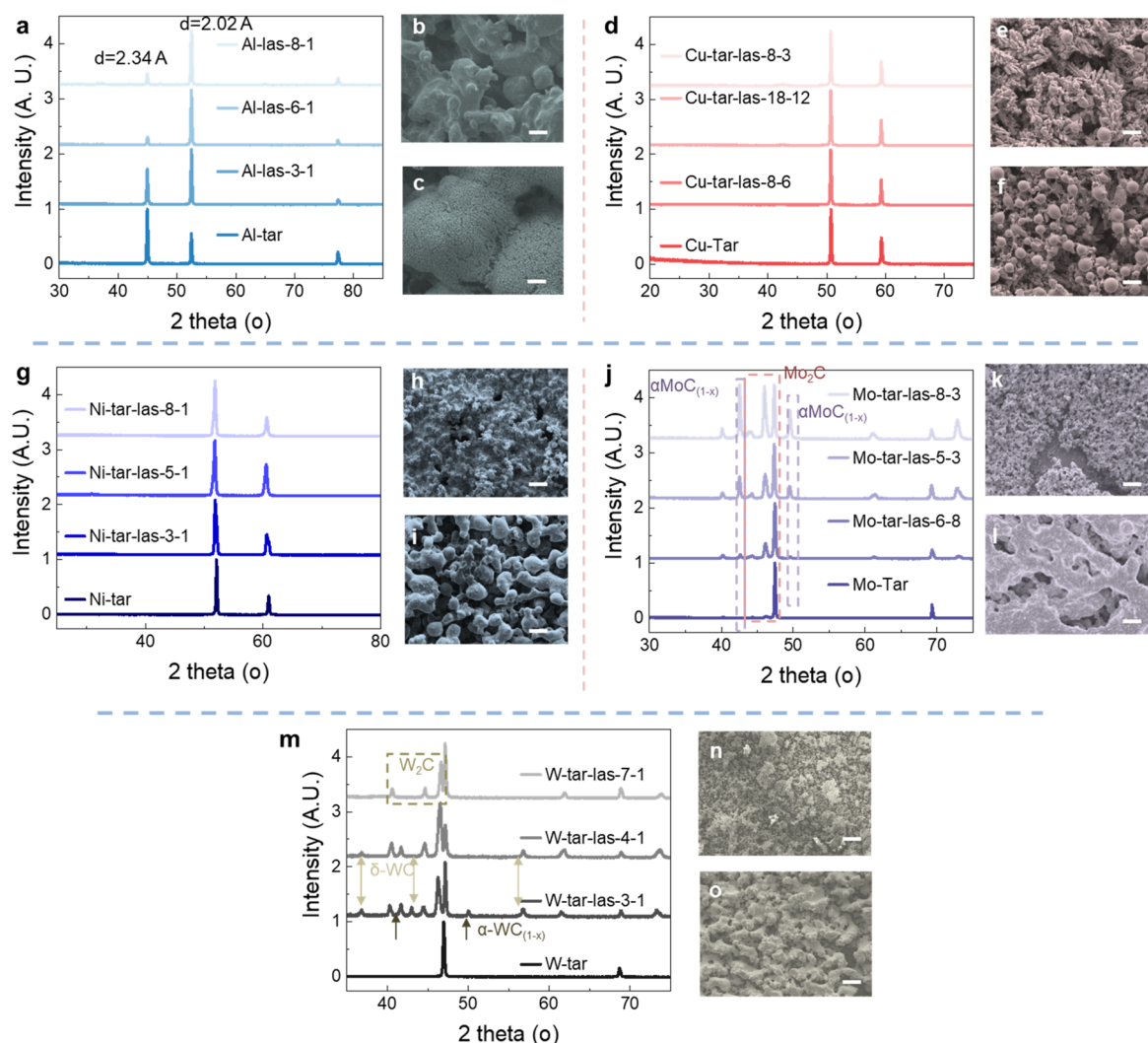


**Figure 2.** Laser-sintered metal and refractory metal phases and microstructures. X-ray diffraction (XRD) pattern of laser-sintered metal–tar thin films and scanning electron micrograph (SEM) of as deposited and laser sintered metal–tar at different laser power and speed, for: (a–c) aluminum-tar; (d–f) copper-tar; (g–i) nickel-tar; (j–l) molybdenum-tar; (m–o) tungsten-tar. XRD in a–c shows the laser-induced sintering leads to a preservation of the metal phases. XRD in (j) and (m) shows the laser sintering process leads to the formation of carbide phases. In a,d,g,j,m, the first number after the “las-” label represents laser power and the second number represents speed in percentages. Scale bars: 10  $\mu\text{m}$ .

process. The peak intensity ratio of  $I_{d=2.02\text{Å}}/I_{d=2.34\text{Å}}$  of Al and laser-sintered Al using 1% rastering speed (12.7 mm/s) and 8% power ( $\sim 2.4$  W) increases from 0.61 to 5.25, indicating a partial ( $\sim 40\%$ ) recrystallization of Fm3m (FCC) phase cubic to Im3m (BCC) cubic Al derived from XRD (Figure S3b). We note that no crystallization is ever observed for Cu, possibly due to the lower internal temperature resulting from a lower carbon content within the carbon–metal interface and with the metal particle itself. With an increase in power/rastering speed ratios, the sizes of the restructured merged Al, Cu and Ni structures increase after sintering, rather than changing the chemical composition (such as forming a carbide phase or oxides in air, Figure S4). The carbon residual in sintered Al, Cu, and Ni thin film should be close to the carbon solid solubility in those metals.

The XRD patterns shown in Figure 2j,m, highlight the formation of carbide phases in both laser-sintered Mo-tar and W-tar films. Higher incident laser power density (power/speed ratio) not only increases the coalition size, but it also applies sufficiently high energy to induce the formation of a mixed

carbide/metal phase. Carbon in tar is oversaturated, which facilitates the formation of metal carbide phases with either  $M_2C$  or  $MC_{(1-x)}$  ( $0 \leq x < 0.5$ ) stoichiometry. As shown in Figure 2j–o and 3 and Figures S5 and S6, with the increase of projected power density, the lower energy  $\beta$ - $Mo_2C$  with lower formation temperature in the Mo–C phase diagram is observed as shown in the carbide I regime. With further increase in incident power up to 2.4 W (at a speed of 40 mm/s), a significant amount (59 at%) of  $\alpha$ - $MoC_{(1-x)}$  is observed as shown in the carbide II regime with 11 at% of molybdenum metal. In the case of tungsten, lower energy phases  $\delta$ -WC and  $\alpha$ - $WC_{(1-x)}$  are observed first. Using 12.7 mm/s as the fixed rastering speed, the  $\beta$ - $W_2C$  phase starts to form in the sintered metal thin film using 0.9 W (3% of power). With higher incident power ( $>1.5$  W), all carbides exhibit the  $\beta$ - $W_2C$  phase. With up to 2.1 W incident power, the sintered tungsten film has 62 atom %  $\beta$ - $W_2C$  phase with 38 atom % metal tungsten. It is worth noting that the carbide phases  $\alpha$ - $MoC_{(1-x)}$  and  $\beta$ - $W_2C$ , which lie in the regime with higher metallurgical formation temperature,

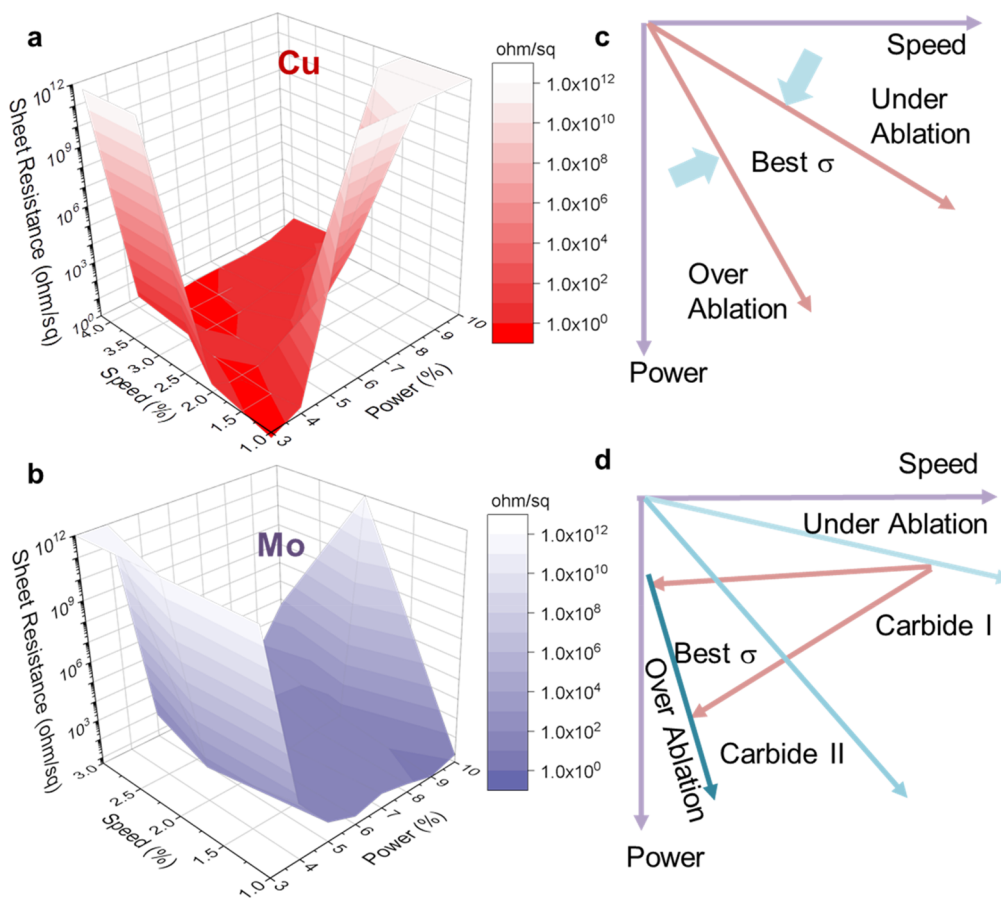


**Figure 3.** Electrical conductivities ( $\sigma$ ) of laser-annealed metal–tar thin films of (a) Cu–tar; (b) Ni–tar; Qualitative depiction of the evolution of: (c) noncarbide metal–tar thin films and (d) formation of carbide phases in refractory metal–tar thin films controlled by laser power and speed. Rastering speed (%) refers to the percentage to the maximum value (1270 mm/s), power (%) refers to the percentage of the full power (30 W).

have higher formation energy than the  $\beta$ - $\text{Mo}_2\text{C}$  phase and  $\delta$ -WC and  $\alpha$ - $\text{WC}_{(1-x)}$  phases.

Beside the crystallographic characterization of laser sintered metal/tar mixtures by XRD, electrical conductivities of sintered films are used to validate the formation of either metallic or carbide phases in refractory metals. Indeed, thin films show different trends in response to the ratio of incident laser power/speed, as shown in Figure 3 and Figure S7. For aluminum, copper and nickel thin films with tar, conductivities are primarily determined by the geometry and connectivity of a percolated single metal phase. The lowest sheet resistance,  $\sim 10^{-1}$  ohm/sq, can be achieved by optimizing the laser power and rastering speed. As shown in Figure 3 and Figures S2–7, metal–tar films are ablated by fixing either the laser power or rastering speed while varying the other. We define the power/scan speed ratio as rastering power density. Figure 3d illustrates the evolution of conductivities with power density. The evolution of metal phases and their microstructures, as well as the electrical conductivity of the resulting thin films follows directly from the incident rastering power density. High speeds and low power results in an “under ablation” regime, while higher power densities result in the increase in interparticle connectivity and conductivity of sintered metal patterns, leading to an optimal regime noted as “highest  $\sigma$ ” in Figure 3c. Further increases in rastering power density into the “over ablation” regime led to severe spheroidization of metal particles and a disconnected percolated network, due to the

metal evaporation under high projected power density (Figures S2–S6). For the formation of carbide phases, the relation between conductivity and power density is more nuanced. As shown in Figure 3d, the regimes of “under ablation” and “over ablation” are characterized by a rastering power density that is either too low to trigger sintering and recrystallization<sup>31</sup> or too high leading to a disruption in the metal percolation network. In the case of Mo and W, the increase of laser power and decrease of scan speed leads to formation of higher energy carbide phases ( $\alpha$ - $\text{MoC}_{(1-x)}$  and  $\beta$ - $\text{W}_2\text{C}$  phase) with interparticle connectivity and thus increased conductivity (Figure 3d and Figures S5 and S6). The high conductivity regime is carbide II, and the conductivity increases while transitioning from carbide phase I to II. In the case of Mo, I–II refers to the  $\beta$ - $\text{Mo}_2\text{C}$  to  $\alpha$ - $\text{MoC}_{(1-x)}$  transition. In the case of W, I–II refers to the  $\alpha$ - $\text{WC}_{(1-x)}$  to  $\beta$ - $\text{W}_2\text{C}$  transition.

The initial size of metal powder in the metal–tar thin film is critical in determining the morphology and conductivity of the as-sintered metal thin film. As shown in Figure S8a–c, Mo–tar thin films are made from tar–metal solution with a mass ratio 100:15:85 (metal/tar/solvent), using smaller powder size ( $\sim 100$  nm) following the same deposition and lasing processes for microsize particles. Those thin films result in much higher sheet resistance ( $10^2$  ohm/sq), while the lasered thin film presents significantly deeper microfractures than laser-ablated Mo–tar using micron size powder (Figure S8d–f). The fractures can be attributed to the larger dewet induced

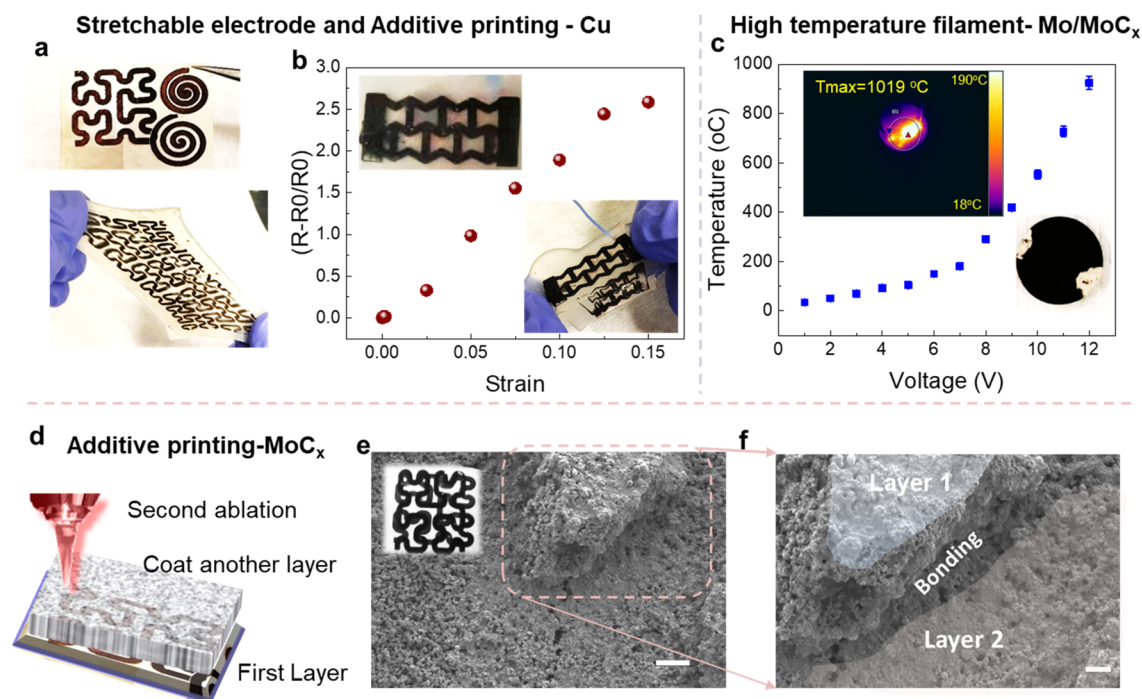


**Figure 4.** Application of laser annealed metal–tar microparticles for thin film electronics. (a) A pattern is printed on as-deposited Cu-tar film and transferred onto Ecoflex. (b) A strain sensor of auxetic copper pattern sandwiched between two layers of Ecoflex. (c) Maximum temperature values of Mo/MoC<sub>x</sub> joule heating filament working in air corresponding as a function of input voltage. Inset, optical image of a joule heater printed on a quartz substrate with 0.5 in. diameter, with the temperature profile powered by a 12 V input voltage. The temperature color map was captured by the infrared camera (FLIR). (d) Schematic of double layer metal printing using tar as absorption binder. (e) SEM image of printed double layer molybdenum carbide, with higher resolution area shown in (f) highlighting the bonding interface between two vertical layers. Scale bar in (e) and (f): 50 and 20  $\mu\text{m}$ .

deformation and shrinking due to merging of particles in the laser sintered metal film, which could be improved by increasing the packing density of metal powder in the tar-metal thin film. To further increase the packing volume fraction,<sup>32</sup> we introduced metal powder with a smaller size ( $\sim 100$  nm) into the  $1\sim 5$   $\mu\text{m}$  size molybdenum powder with a mass ratio of 1:1 to make a Mo(mix)–tar solution with the same mass ratio of tar and solvent in monosize tar–metal solutions. Laser sintered Mo(mix)–tar showed clear improvement compared to sintered Mo–tar using monodistributed micron size particles, displaying fewer visible cracks, and slightly lower sheet resistance—decreased from 4.1 to 3.0 ohm/sq (Figure S8g–i).

We show next that devices can be fabricated through patterning using the optimized laser parameters that give the highest conductivity (supplementary notes). Laser annealing with high spatial resolution can be used to tailor the device geometry on temperature-sensitive substrates such as polyimide. Residual unlasered copper-tar is washed off using dichloromethane (DCM) (Figure 4a). The laser-sintered copper pattern can be transferred onto flexible substrates such as Ecoflex to fabricate stretchable electronic devices, in this case a strain sensor (Figure 4b). The resistance of the as-printed auxetic pattern shows a linear response with applied strain up to 0.15, with a gauge factor  $\sim 20$ , which is much higher than the elasticity limit of copper metal.<sup>33</sup> The auxetic pattern and the interconnected porous copper microstructures enables the repetitive application of large strains beyond 150 cycles (Figure S9). Laser annealing a Mo/MoC<sub>x</sub> in a wire form-factor, shows low resistivity down to 0.5 ohm/sq, making it an ideal candidate for a Joule heating filament.<sup>34</sup> Figure 4c

shows that in such an application, the filament can reach up to  $\sim 1000$  °C in open air with an input voltage of 12 V.

The viability of the laser-sintering process in additive manufacturing is tested by synthesizing a vertical sintered double layer. Here, a layer-by-layer coating and printing is achieved through repeated sequences of depositions, patterning, laser annealing, and residual washing off. While residual carbon on the laser-sintered Cu and Al thin films will block the formation of interlayer bonding, carbide formation in Mo–tar and W–tar could potentially bond the two layers. As a proof of concept, a double layer of a Mo/MoC<sub>x</sub> pattern is demonstrated in Figure 4d–f. After removing the residual powder, the bonding between the two layers of Mo/MoC<sub>x</sub> can be seen from the SEM of Figure 4f. The first layer molybdenum sintering is performed using low power (1.8 W) and low rastering speed (12.7 mm/s) to increase the packing density of the sintered structure. The second layer is sintered with relatively high power ( $\sim 4.5$  W) and a rastering speed of (101.6 mm/s) to increase the penetration depth and interlayer bonding. Such a result indicates the potential of extending the tar mediated laser sintering of metal carbide formation into additive printing processes.

## CONCLUSION

In summary, we present tar-mediated laser sintering of metal nano- and microparticles including Al, Cu, Ni, and refractory Mo and W using relatively low power ( $< 2$  W) under ambient conditions. A thin layer of carbon segregates on aluminum and copper sintered films surface due to its low solubility in these metals,<sup>25</sup> while nickel with higher carbon solubility provides a clean surface after laser annealing.<sup>28</sup> Refractory metals

(molybdenum and tungsten) which are laser sintered in air, result in different high energy transition metal carbide phases,<sup>29,30</sup> through optimized control over laser power and rastering speed. By exploiting the microstructure and high electrical conductivity of the laser sintered metal and metal carbide thin films, we demonstrate the successful fabrication of a strain sensor with a laser-printed copper auxetic pattern with linearity behavior up to 15% strain, and a gauge factor of  $\sim 20$ . Laser printed Mo/MoC<sub>x</sub> Joule heating filaments are also fabricated with a sheet resistance below 1.6 ohm/sq, leading to an operational maximum temperature over 1000 °C in the open air with an input power of 12 V. Furthermore, we demonstrated a proof-of-concept sequential multilayer printing process of molybdenum carbide, with a method that can be potentially expanded and integrated into additive manufacturing processes.

Most importantly, with the assistance of an absorbing binder the input energy is 2 orders of magnitude smaller than what is required in other metal printing methods such as selective laser melting (SLM)<sup>4,35,36</sup> and electron beam melting (EBM).<sup>37,38</sup> Without using tar in the metal thin film, the low power down to 1W cannot trigger any photon-induced thermal reactions. Furthermore, the laser-induced metal sintering method here proposed operates under ambient conditions, eliminating the need for ventilation and pumping, in turn decreasing the processing time and complexity compared to SLM and EBL. Direct laser printing in air through a compact laser source reduces the processing overhead imposed by the otherwise required control over the buffer gas during annealing and instrumental complexity in the case of EBM. Such factors could potentially reduce the complexity of fabricating metal and metal carbide films in continuous “roll-to-roll” manufacturing. Furthermore, the tar–metal ink could potentially be adapted to an extrusion-based 3D printer with fiber optics and, thus, be done in an additive way of printing.

## MATERIALS AND METHODS

**Materials.** Stream cracked tar was provided by ExxonMobil (Defluxed SOP2 Tar from 15 to 082837). Aluminum powder (1–5  $\mu\text{m}$ ) and copper powder (<45  $\mu\text{m}$ ) were purchased from Sigma-Aldrich. Nickel powder (3–7  $\mu\text{m}$ ), molybdenum powder (2–4  $\mu\text{m}$ ), and tungsten powder (1–5  $\mu\text{m}$ ) were all purchased from Alfa Aesar. Dichloromethane (DCM, CAS 75–09–2) was purchased from Sigma-Aldrich.

**Materials Analysis and Characterization.** A profilometer (Bruker DXT Stylus Profilometer) was used to map the thickness of spin coated and laser ablated thin films. Scanning electron microscopy (SEM, Hitachi SU8100) was used to image the laser sintered metal–tar thin films. Energy-dispersive X-ray spectroscopy (EDX) mapping was taken in SEM using an Oxford EDX detector (15 kV, 20  $\mu\text{m}$ ) controlled by an APEX software interface. Micro-Raman spectra were acquired using a Renishaw inVia confocal Raman microscope using a 473 nm excitation source. The laser spot on the sample was  $\sim 800$  nm in diameter and had a power of  $\sim 4$  mW at the sample surface. The full spectral window for each acquisition is from 600 to 3200  $\text{cm}^{-1}$ . X-ray diffraction patterns of metal–tar thin films were tested using the Bruker D8 Discovery, and semiquantitative analysis of patterns was performed using HighScore software to identify the phases and estimate the components.

**Laser Sintering of Metal–Tar Thin Film.** A tar solution (15 wt %) was made by diluting as received tar by dichloromethane (DCM). Thin films were created by spin coating a suspension of metal powder in the tar solution with mass ratio 100:15:85 (metal/tar/solvent). Metal powders and their physical properties are summarized in Table S1. The tar solution was spun coated onto glass substrates at a speed of 500 rpm for 20 s, and the deposited metal–tar thin films were dried

in air for 4 h and heated up to 80 °C to remove the volatile component and residual solvent. A commercial laser cutter (Universal VSL 2.30) was utilized to perform the laser annealing and sintering with a CO<sub>2</sub> laser tube (maximum power of 30W) and all built-in optics. The laser spot was focused on the top surface of the spin-coated films by tuning the z-position (height) of the supporting cutting table. The designed pattern was imported to a vector graphics software (Inkscape) and engraved by communicating with the laser cutter as a printer. On different metal–tar thin films, different parameters of power and speed were crossed compared for maximum conductivity at focus.

**Prototyping Laser Sintered Metal Devices.** To prototype more complex designs for metal devices, the laser was calibrated to the parameters that achieved the highest conductivity. Using a computer aid design (CAD) interface, many features were directly printed on tar-metal film. As-ablated devices were rinsed in solvent DCM to remove the unablated areas, and air-dried followed with heat up to 100 °C to fully remove solvent. Copper-tar printed in the patterns in Figure 4a are sintered by laser annealing and washed with solvent to remove residual copper powder and transferred onto Ecoflex to make a stretchable strain sensor.

**Conductivity Measurement.** A lakeshore TTP4 probe station was used for sheet resistance characterization. Parameter analyzer (4156C) is interfaced with a PC running EasyExpert software to setup any test with up to 1 mA and 5 V. All room-temperature electrical characterization was done in air.

**Testing of the Mo/MoC<sub>1-x</sub> Filament.** Mo–tar thin films were deposited onto quartz substrates of 0.5-in. diameter. Laser sintering was performed as described above with the calibrated power and speed parameters with the highest resulting conductivity. Two electrodes were deposited using silver paste on the edge of the Mo/MoC<sub>x</sub> thin film. The heating performance of the filament was tested using a DC voltage source, ranging from 1 to 12 V with a step of 1 V. At each voltage input, the temperature was recorded by an IR camera (FLIR A 615) for 10 min until the temperature saturated.

## ASSOCIATED CONTENT

### Supporting Information

The Supporting Information is available free of charge at <https://pubs.acs.org/doi/10.1021/acsnano.0c04295>.

Physical and optical properties of tar and metals tested, simulation set up of tar, SEMs of laser sintered metal–tar thin films, conductivities ( $\sigma$ ) of laser annealed metal–tar thin films, and a demonstration of strain sensor made of laser sintered copper(PDF)

## AUTHOR INFORMATION

### Corresponding Author

Jeffrey C. Grossman – Department of Materials Science and Engineering, Massachusetts Institute of Technology, Cambridge, Massachusetts 02139, United States; [orcid.org/0000-0003-1281-2359](https://orcid.org/0000-0003-1281-2359); Email: [jcg@mit.edu](mailto:jcg@mit.edu)

### Authors

Xining Zang – Department of Materials Science and Engineering, Massachusetts Institute of Technology, Cambridge, Massachusetts 02139, United States; [orcid.org/0000-0001-6930-8060](https://orcid.org/0000-0001-6930-8060)

Kiera Y. Tai – Department of Materials Science and Engineering, Massachusetts Institute of Technology, Cambridge, Massachusetts 02139, United States

Cuiying Jian – Department of Materials Science and Engineering, Massachusetts Institute of Technology, Cambridge, Massachusetts 02139, United States; Department of Mechanical Engineering, York University, Toronto, ON M3J 1P3, Canada; [orcid.org/0000-0003-0138-6550](https://orcid.org/0000-0003-0138-6550)

Wan Shou – Computer Science and Artificial Intelligence Laboratory, Massachusetts Institute of Technology, Cambridge, Massachusetts 02139, United States

Wojciech Matusik – Computer Science and Artificial Intelligence Laboratory, Massachusetts Institute of Technology, Cambridge, Massachusetts 02139, United States

Nicola Ferralis – Department of Materials Science and Engineering, Massachusetts Institute of Technology, Cambridge, Massachusetts 02139, United States

Complete contact information is available at:  
<https://pubs.acs.org/10.1021/acsnano.0c04295>

### Author Contributions

X.Z. and J.C.G. designed the research; X.Z. designed and performed experiments; K.Y.T. helped with metal sintering; C. J. performed the simulation; W.S. helped with the test of printed sensors; N.F. provided insight on tar chemistry, film and process characterization; X.Z., N.F. and J.C.G. wrote the paper; all the authors provided comments and feedback on the manuscript.

### Notes

The authors declare no competing financial interest.

### ACKNOWLEDGMENTS

The tar used in this work was provided by ExxonMobil. This work made use of the MRSEC Shared Experimental Facilities at MIT, supported by the National Science Foundation under Award No. DMR-14-19807.

### REFERENCES

- (1) Antusch, S.; Reiser, J.; Hoffmann, J.; Onea, A. Refractory Materials for Energy Applications. *Energy Technol.* **2017**, *5*, 1064–1070.
- (2) Pierson, H. O. Carbides of Group VI. In *Handbook of Refractory Carbides and Nitrides*; William Andrew, Inc.: New York, 1996; pp 100–117.
- (3) Prakash, L. J. Application of Fine Grained Tungsten Carbide Based Cemented Carbides. *Int. J. Refract. Hard Met.* **1995**, *13*, 257–264.
- (4) Mercelis, P.; Kruth, J. Residual Stresses in Selective Laser Sintering and Selective Laser Melting. *Rapid Prototyp. J.* **2006**, *12*, 254–265.
- (5) Visser, C. W.; Pohl, R.; Sun, C.; Römer, G.-W.; Huis in 't Veld, B.; Lohse, D. Toward 3D Printing of Pure Metals by Laser-Induced Forward Transfer. *Adv. Mater.* **2015**, *27*, 4087–4092.
- (6) Wang, Y. M.; Voisin, T.; McKeown, J. T.; Ye, J.; Calta, N. P.; Li, Z.; Zeng, Z.; Zhang, Y.; Chen, W.; Roehling, T. T.; Ott, R. T.; Santala, M. K.; Depond, P. J.; Matthews, M. J.; Hamza, A. V.; Zhu, T. Additively Manufactured Hierarchical Stainless Steels with High Strength and Ductility. *Nat. Mater.* **2018**, *17*, 63–71.
- (7) Kenel, C.; Casati, N. P. M.; Dunand, D. C. 3D Ink-Extrusion Additive Manufacturing of CoCrFeNi High-Entropy Alloy Micro-Lattices. *Nat. Commun.* **2019**, *10*, 904.
- (8) Prasad, K.; Bazaka, O.; Chua, M.; Rochford, M.; Fedrick, L.; Spoor, J.; Symes, R.; Tieppo, M.; Collins, C.; Cao, A.; Markwell, D.; Ostrikov, K.; Bazaka, K. Metallic Biomaterials: Current Challenges and Opportunities. *Materials* **2017**, *10*, 884.
- (9) Antusch, S.; Reiser, J.; Hoffmann, J.; Onea, A. Refractory Materials for Energy Applications. *Energy Technol.* **2017**, *5*, 1064–1070.
- (10) Penilla, E. H.; Devia-Cruz, L. F.; Wieg, A. T.; Martinez-Torres, P.; Cuando-Espitia, N.; Sellappan, P.; Kodera, Y.; Aguilar, G.; Garay, J. E. Ultrafast Laser Welding of Ceramics. *Science (Washington, DC, U. S.)* **2019**, *365*, 803–808.
- (11) El-Kady, M. F.; Kaner, R. B. Scalable Fabrication of High-Power Graphene Micro-Supercapacitors for Flexible and on-Chip Energy Storage. *Nat. Commun.* **2013**, *4*, 1475.
- (12) Zang, X.; Jian, C.; Ingersoll, S.; Li, H.; Adams, J. J.; Lu, Z.; Ferralis, N.; Grossman, J. C. Laser-Engineered Heavy Hydrocarbons: Old Materials with New Opportunities. *Sci. Adv.* **2020**, *6*, No. eaaz5231.
- (13) Tan, K. W.; Jung, B.; Werner, J. G.; Rhoades, E. R.; Thompson, M. O.; Wiesner, U. Transient Laser Heating Induced Hierarchical Porous Structures from Block Copolymer-Directed Self-Assembly. *Science (Washington, DC, U. S.)* **2015**, *349*, 54–58.
- (14) Zang, X.; Jian, C.; Zhu, T.; Fan, Z.; Wang, W.; Wei, M.; Li, B.; Follmar Diaz, M.; Ashby, P.; Lu, Z.; Chu, Y.; Wang, Z.; Ding, X.; Xie, Y.; Chen, J.; Hohman, J. N.; Sanghadasa, M.; Grossman, J. C.; Lin, L. Laser-Sculptured Ultrathin Transition Metal Carbide Layers for Energy Storage and Energy Harvesting Applications. *Nat. Commun.* **2019**, *10*, 3112.
- (15) Zang, X.; Shen, C.; Chu, Y.; Li, B.; Wei, M.; Zhong, J.; Sanghadasa, M.; Lin, L. Laser-Induced Molybdenum Carbide-Graphene Composites for 3D Foldable Paper Electronics. *Adv. Mater.* **2018**, *30*, 1800062.
- (16) Frazier, W. E. Metal Additive Manufacturing: A Review. *J. Mater. Eng. Perform.* **2014**, *23*, 1917–1928.
- (17) Wu, D.; Liu, H.; Lu, F.; Ma, G.; Yan, S.; Niu, F.; Guo, D. Al<sub>2</sub>O<sub>3</sub>-YAG Eutectic Ceramic Prepared by Laser Additive Manufacturing with Water-Cooled Substrate. *Ceram. Int.* **2019**, *45*, 4119–4122.
- (18) Eckel, Z. C.; Zhou, C.; Martin, J. H.; Jacobsen, A. J.; Carter, W. B.; Schaedler, T. A. Additive Manufacturing of Polymer-Derived Ceramics. *Science (Washington, DC, U. S.)* **2016**, *351*, 58–62.
- (19) Babar, S.; Weaver, J. H. Optical Constants of Cu, Ag, and Au Revisited. *Appl. Opt.* **2015**, *54*, 477.
- (20) Ordal, M. A.; Bell, R. J.; Alexander, R. W.; Long, L. L.; Querry, M. R. Optical Properties of Fourteen Metals in the Infrared and Far Infrared: Al, Co, Cu, Au, Fe, Pb, Mo, Ni, Pd, Pt, Ag, Ti, V, and W. *Appl. Opt.* **1985**, *24*, 4493.
- (21) Ordal, M. A.; Long, L. L.; Bell, R. J.; Bell, S. E.; Bell, R. R.; Alexander, R. W.; Ward, C. A. Optical Properties of the Metals Al, Co, Cu, Au, Fe, Pb, Ni, Pd, Pt, Ag, Ti, and W in the Infrared and Far Infrared. *Appl. Opt.* **1983**, *22*, 1099.
- (22) Ordal, M. A.; Bell, R. J.; Alexander, R. W.; Newquist, L. A.; Querry, M. R. Optical Properties of Al, Fe, Ti, Ta, W, and Mo at Submillimeter Wavelengths. *Appl. Opt.* **1988**, *27*, 1203.
- (23) Alcañiz-Monge, J.; Cazorla-Amorós, D.; Linares-Solano, A. Characterisation of Coal Tar Pitches by Thermal Analysis, Infrared Spectroscopy and Solvent Fractionation. *Fuel* **2001**, *80*, 41–48.
- (24) Mizuno, K.; Ishii, J.; Kishida, H.; Hayamizu, Y.; Yasuda, S.; Futaba, D. N.; Yumura, M.; Hata, K. A Black Body Absorber from Vertically Aligned Single-Walled Carbon Nanotubes. *Proc. Natl. Acad. Sci. U. S. A.* **2009**, *106*, 6044–6047.
- (25) López, G. A.; Mittemeijer, E. J. The Solubility of C in Solid Cu. *Scr. Mater.* **2004**, *51*, 1–5.
- (26) Li, X.; Cai, W.; An, J.; Kim, S.; Nah, J.; Yang, D.; Piner, R.; Velamakanni, A.; Jung, I.; Tutuc, E.; Banerjee, S. K.; Colombo, L.; Ruoff, R. S. Large-Area Synthesis of High-Quality and Uniform Graphene Films on Copper Foils. *Science (Washington, DC, U. S.)* **2009**, *324*, 1312–1314.
- (27) Klinke, D. J.; Wilke, S.; Broadbelt, L. J. A Theoretical Study of Carbon Chemisorption on Ni(111) and Co(0001) Surfaces. *J. Catal.* **1998**, *178*, 540–554.
- (28) Singleton, M.; Nash, P. The C-Ni (Carbon-Nickel) System. *Bull. Alloy Phase Diagrams* **1989**, *10*, 121–126.
- (29) Hugosson, H. W.; Eriksson, O.; Nordström, L.; Jansson, U.; Fast, L.; Delin, A.; Wills, J. M.; Johansson, B. Theory of Phase Stabilities and Bonding Mechanisms in Stoichiometric and Substoichiometric Molybdenum Carbide. *J. Appl. Phys.* **1999**, *86*, 3758–3767.
- (30) Kurlov, A. S.; Gusev, A. I. Tungsten Carbides and W-C Phase Diagram. *Inorg. Mater.* **2006**, *42*, 121–127.

- (31) Sugiyama, T.; Masuhara, H. Laser-Induced Crystallization and Crystal Growth. *Chem. - Asian J.* **2011**, *6*, 2878–2889.
- (32) Shi, Y.; Zhang, Y. Simulation of Random Packing of Spherical Particles with Different Size Distributions. *Appl. Phys. A: Mater. Sci. Process.* **2008**, *92*, 621–626.
- (33) Ledbetter, H. M.; Naimon, E. R. Elastic Properties of Metals and Alloys. II. Copper. *J. Phys. Chem. Ref. Data* **1974**, *3*, 897–935.
- (34) Okoli, S.; Haubner, R.; Lux, B. Carburization of Tungsten and Tantalum Filaments during Low-Pressure Diamond Deposition. *Surf. Coat. Technol.* **1991**, *47*, 585–599.
- (35) Kruth, J.; Mercelis, P.; Van Vaerenbergh, J.; Froyen, L.; Rombouts, M. Binding Mechanisms in Selective Laser Sintering and Selective Laser Melting. *Rapid Prototyp. J.* **2005**, *11*, 26–36.
- (36) Kumar, S. Selective Laser Sintering/Melting. In *Comprehensive Materials Processing*; Elsevier, Ltd., 2014; *10*, pp 93–134.
- (37) Murr, L. E.; Gaytan, S. M.; Ramirez, D. A.; Martinez, E.; Hernandez, J.; Amato, K. N.; Shindo, P. W.; Medina, F. R.; Wicker, R. B. Metal Fabrication by Additive Manufacturing Using Laser and Electron Beam Melting Technologies. *J. Mater. Sci. Technol.* **2012**, *28*, 1–14.
- (38) Rafi, H. K.; Karthik, N. V.; Gong, H.; Starr, T. L.; Stucker, B. E. Microstructures and Mechanical Properties of Ti6Al4V Parts Fabricated by Selective Laser Melting and Electron Beam Melting. *J. Mater. Eng. Perform.* **2013**, *22*, 3872–3883.